X International Conference on Computational Methods in Marine Engineering
MARINE 2023
J. García-Espinosa, L. González, J.E. Gutiérrez & B. Serván-Camas (Eds)

Comparison of RANS Turbulence Models for the Simulation of Smooth Wall Boundary-Layers in Pressure Gradients at Moderate and High Reynolds Numbers

L.Eça*, M.Kerkvliet† and S.L.Toxopeus†

*MARIN Academy, Instituto Superior Técnico (IST), ULisbon
Av. Rovisco Pais 1, 1049-001 Lisboa, Portugal
e-mail: luis.eca@tecnico.ulisboa.pt

† Maritime Research Institute Netherlands (MARIN)
Haagsteeg 2, 6708 PM Wageningen, The Netherlands
e-mail: M.Kerkvliet@marin.nl, S.L.Toxopeus@marin.nl

Abstract

In this work, our focus is to assess the effect of the Reynolds number on the performance of six different RANS turbulence models in the simulation of viscous flows. To this end, we have selected the experiments performed in a wind tunnel at Virginia Tech that measured boundary-layers in favorable and adverse pressure gradients. A rectangular wing with a NACA 0012 section placed in the middle of the wind tunnel at angles of attack ranging between -10 and 12 degrees is used to induce the pressure gradient.

The two-dimensional computational domain proposed for the comparison with the experimental data is used to simulate the flows at Reynolds numbers of $Re = 2 \times 10^6$ (model scale, applicable to the wind tunnel tests) and $Re = 10^9$ (representative for full scale conditions) with the wing at angles of attack of -10, 0 and 12 degrees. Calculations are performed with a RANS solver using five eddy-viscosity models and a Reynolds-stress model. Differences between the solutions obtained with the six turbulence models are quantified for several quantities of interest including force coefficients, shear-stress and pressure coefficients, mean velocities, turbulence kinetic energy and Reynolds stresses using point-wise and global Validation metrics.

For the present test cases, discrepancies between solutions of the six selected turbulence models at model scale Reynolds number are significantly larger than those observed at full scale Reynolds number. Therefore, modeling error assessments (validation) performed at model scale Reynolds number cannot be extrapolated to full scale.

Keywords: RANS Turbulence models; Reynolds number effects; CFD

1. INTRODUCTION

Currently, there is an ongoing international collaboration through the North Atlantic Treaty Organization (NATO) Science & Technology Organization (STO) Applied Vehicle Technology (AVT) 349 Research Task Group (RTG) on Non-Equilibrium Turbulent Boundary Layers in High Reynolds Number Flow at Incompressible Conditions. Several two-dimensional and three-dimensional test cases have been selected including smooth and rough walls. One of these test cases is taken from the experimental measurements of boundary-layers under non-equilibrium pressure gradients that have been performed at Virginia Tech, Fritsch et al. [2020]. The pressure gradient imposed to the boundary-layers is induced by a rectangular wing with a NACA 0012 section placed in the middle of a wind tunnel at angles of attack ranging between -10 and 12 degrees.

A comparison of simulations performed by several flow solvers based on the Reynolds-averaged Navier-Stokes (RANS) equations using different turbulence models with the experimental data

has been reported by Fritsch et al. [2022]. The study presented by Fritsch et al. [2022] assumed a two-dimensional geometry and the proposed computational domain included a tilted top wall to take into account the displacement thickness of the side walls boundary-layers. The Reynolds number based on the velocity of the incoming flow V_∞, airfoil chord c and fluid kinematic viscosity ν is $Re = 2 \times 10^6$, which for most naval applications corresponds to model scale. Although these validation exercises provide useful information about the modeling accuracy of RANS and the available turbulence models, it is not guaranteed that full scale flows will exhibit the same trends. Therefore, the goal of the present study is to assess the performance of RANS at full scale Reynolds numbers, which for ship flows is typically of the order of $Re = 10^9$.

In the absence of experimental data at full scale Reynolds number, a first quantitative assessment of the influence of the turbulence model on the accuracy of viscous flow simulations can be performed using point-wise V&V20 [2009] and global V&V20.1 [2023] Validation metrics. Using one of the turbulence models solution as the reference ("experimental data"), it is possible to quantity the discrepancies between the solutions obtained with different turbulence models. Therefore, it is possible to compare the influence of the turbulence model on the results of the RANS simulations at model and full scale Reynolds numbers.

To this end, we have selected the experiments reported by Fritsch et al. [2020] at angles of attack of -10, 0 and 12 degrees and the two-dimensional domain proposed by Fritsch et al. [2022] to calculate the flows at Reynolds numbers of $Re = 2 \times 10^6$ and $Re = 10^9$. Simulations are performed with a RANS solver using six turbulence models including five eddy-viscosity models and a Reynolds-stress model.

Quantities of interest include flow quantities from the boundary-layer on the wind tunnel wall and from the airfoil surface. For the wall boundary-layer, we have selected pressure and skin friction coefficients distributions, boundary-layer integral parameters and mean velocity, turbulence kinetic energy and Reynolds shear-stress profiles. Friction and pressure force coefficients and pressure and skin friction distributions are analyzed for the airfoil. Integral quantities are easily addressed with the point-wise metric of V&V20 [2009], whereas the global metric of V&V20.1 [2023] is more appropriate for distributions and profiles.

The remainder of this paper is organized in the following way: Section 2 presents the mathematical model; the flow solver is briefly presented in Section 3 and the Validation metrics are described in Section 4; Section 5 presents the test cases including the computational domain, boundary conditions, grid sets and numerical details; the results are presented and discussed in Section 6 and the main conclusions of this work are summarized in Section 7.

2. MATHEMATICAL MODEL

The Reynolds-averaged mass conservation and momentum balance equations for a statistically steady flow of a Newtonian incompressible fluid (constant density, ρ) can be written in a ($x_i \equiv x, y, z$) Cartesian coordinate system as

$$\begin{aligned} \frac{\partial V_i}{\partial x_i} &= 0, \\ \frac{\partial \left(V_i V_j \right)}{\partial x_j} &= -\frac{1}{\rho} \frac{\partial P}{\partial x_i} + \frac{1}{\rho} \frac{\partial \tau_T}{\partial x_j} \, , \\ \frac{\tau_T}{\rho} &= \nu \left(\frac{\partial V_i}{\partial x_j} + \frac{\partial V_j}{\partial x_i} \right) - \overline{v_i v_j} \, . \end{aligned} \tag{1}$$

V_i and P are the mean values of the Cartesian velocity components and mean relative pressure, respectively. τ_T is the total stress tensor and v_i are the fluctuating part (turbulence) of the Cartesian velocity components and the over-bar designates time-averaging. The Reynolds stress tensor $-\rho\overline{v_i v_j}$ requires a turbulence model to close the problem.

2.1 Turbulence models

In this work we have selected six turbulence models including five based on the so-called Boussinesq approximation that determines the Reynolds stress tensor as a function of the mean strain

rate and the eddy-viscosity ν_t

$$-\overline{v_i v_j} = \nu_t \left(\frac{\partial V_i}{\partial x_j} + \frac{\partial V_j}{\partial x_i} \right) - \frac{2}{3}\delta_{ij} k \ , \tag{2}$$

where k is the turbulence kinetic energy and δ_{ij} is the Kronecker symbol. The contribution of k to the normal stresses is absorbed in the mean pressure gradient term. The sixth model calculates directly the components of the Reynolds stress tensor.

The five eddy-viscosity models selected for this study are: the one-equation Spalart and Allmaras [1992] model (SPAL); two versions of the two-equation, Shear-Stress Transport $k-\omega$ model proposed by Menter [1994] (SST94) and Menter et al. [2003] (SST03); the two-equation Turbulent Non-Turbulent $k-\omega$ model presented by Kok [2000] (TNT) and the two-equation $k-\sqrt{k}L$ described in Menter et al. [2006] (KSKL). All these turbulence models include a transport equation for the turbulence kinetic energy k with the exception of the SPAL model that solves a transport equation for an undamped eddy-viscosity. For the SPAL model, k is determined from

$$k = \frac{\nu_t S}{\sqrt{c_\mu}} \ , \tag{3}$$

where S is the magnitude of the mean-strain rate and $c_\mu = 0.09$.

The SSG/LRR$-\omega$ Reynolds-Stress model (RSM) proposed in Eisfeld et al. [2016] solves seven transport equations to determine six components of the Reynolds stress tensor (the tensor is symmetric) and ω. Therefore, this model does not rely on the eddy-viscosity to determine the Reynolds stresses. Nonetheless, the model still requires the calculation of the eddy-viscosity to solve the ω transport equation. The turbulence kinetic energy is obtained from its definition:

$$k = \frac{1}{2}\left(\overline{v_x^2} + \overline{v_y^2} + \overline{v_z^2} \right) \ . \tag{4}$$

3. FLOW SOLVER

All simulations were performed with ReFRESCO that is a flow solver based on a finite volume discretization of the continuity and momentum equations written in strong conservation form. The solver uses a fully-collocated arrangement and a face-based approach that enables the use of cells with an arbitrary number of faces. Picard linearization is applied to the convective terms of the transport equations and mass conservation is ensured using a SIMPLE-like algorithm, described for example by Klaij and Vuik [2013], and a pressure-weighted interpolation technique to avoid spurious oscillations as proposed in Miller and Schmidt [1988]. Thorough code verification is performed for all releases of ReFRESCO, as illustrated in Eça et al. [2016].

In the present study, a segregated approach was adopted for all simulations, which means that momentum, pressure correction (mass conservation) and turbulence equations are solved sequentially for each non-linear iteration.

Second-order schemes are applied to all terms of the transport equations with the exception of the convective terms of the turbulence models transport equations that are approximated by first-order upwind. Effect of this choice has been investigated in Eça et al. [2022] for the SPAL and SST03 turbulence models: similar numerical uncertainties were obtained for most quantities of interest using first or second-order upwind in the convective terms of the SPAL and SST03 turbulence models. In the attached boundary-layers addressed in this study, the increase of robustness of the flow solver justifies the use of first-order upwind in the turbulence quantities transport equations.

4. VALIDATION METRICS

The Validation metric presented in V&V20 [2009] determines an interval that should contain the modeling error of a point-wise quantity of interest obtained from the numerical solution of a mathematical/computational model $S(\phi)$. The interval is centered at the difference between $S(\phi)$ and the corresponding experimental data $D(\phi)$ (comparison error), and it has a width (validation uncertainty) that depends on the experimental, numerical and input uncertainties.

This metric can also be used to quantify differences between solutions determined with different turbulence models. The solution obtained with one turbulence model is used as the "experimental data", i.e. as the reference $S_{\text{ref}}(\phi)$, to determine

$$\Delta_{\text{tm}}(\phi) = S(\phi) - S_{\text{ref}}(\phi) \ . \tag{5}$$

The simulations are affected by numerical uncertainties and input parameters uncertainties. However, it is reasonable to assume that input uncertainties are equivalent for both simulations when $S(\phi)$ and $S_{\text{ref}}(\phi)$ are obtained with the same boundary conditions and fluid properties. Therefore, the uncertainty in the determination of $\Delta_{\text{tm}}(\phi)$ depends only on the numerical uncertainties $U_S(\phi)$ and $U_{S_{\text{ref}}}(\phi)$ that can be combined to determine

$$U_{\Delta_{\text{tm}}}(\phi) = \sqrt{\left(U_S(\phi)\right)^2 + \left(U_{S_{\text{ref}}}(\phi)\right)^2} \ . \tag{6}$$

The interval that should contain the difference between the solutions of the two turbulence models, $\delta_{\text{tm}}(\phi)$ is defined by

$$\Delta_{\text{tm}}(\phi) - U_{\Delta_{\text{tm}}}(\phi) \leq \delta_{\text{tm}}(\phi) \leq \Delta_{\text{tm}}(\phi) + U_{\Delta_{\text{tm}}}(\phi) \ . \tag{7}$$

When there are many quantities of interest, as for example for the skin friction or pressure distribution along a surface, the interpretation of the results obtained from equation (7) is not easy. A simple way to quantify globally the discrepancies between the solutions of two turbulence models is to calculate the multivariate metric presented in V&V20.1 [2023]:

$$\Delta^2_{\text{mv}} = {\boldsymbol{\Delta}_{\text{tm}}}^T {\mathbf{V}_{\text{val}}}^{-1} \boldsymbol{\Delta}_{\text{tm}} \ , \tag{8}$$

where $\boldsymbol{\Delta}_{\text{tm}}$ is an array with the n_p evaluations (set-points) of the differences $\Delta_{\text{tm}}(\phi)_i$ and $\mathbf{V}_{\text{val}}$ is the co-variance matrix that is dependent only on the numerical uncertainties. Assuming that $U_S(\phi)_i$ and $U_{S_{\text{ref}}}(\phi)_i$ at the n_p set-points are independent, $\mathbf{V}_{\text{val}}$ is a diagonal matrix with each entry equal to $U_{\Delta_{\text{tm}}}(\phi)_i$. Furthermore, normalizing the results with the expected value of $\Delta^2_{\text{ref}} = n_p$ V&V20.1 [2023] leads to

$$\frac{\Delta_{\text{mv}}}{\Delta_{\text{ref}}} = \sqrt{\frac{1}{n_p} \sum_{i=1}^{n_p} \frac{\left(\Delta_{\text{tm}}(\phi)_i\right)^2}{\left(U_{\Delta_{\text{tm}}}(\phi)_i\right)^2}} \ . \tag{9}$$

If $\Delta_{\text{mv}}/\Delta_{\text{ref}} \leq 1$ the differences between the solutions obtained with the two turbulence models are within the error bars generated by the numerical uncertainties and so it is not possible to take quantitative conclusions, i.e. this means that the two solutions do not differ significantly if the validation uncertainty is small.

5. TEST CASE

5.1 Computational domain and flow parameters

The Virginia Tech Stability Wind Tunnel (VTSWT) has a square cross section of $(1.85 \times 1.85\text{m})$ and a wing with a NACA 0012 section of 0.914m chord is installed horizontally at mid height in the test section center and swept to various angles of attack between $-10°$ and $12°$, as illustrated in the left plot of Figure 1 taken from Fritsch et al. [2022]. In the experiments, the boundary-layer of interest develops on the bottom wall and the pressure gradient imposed to the boundary-layer is controlled by the angle of attack at which the wing is positioned.

The simulations performed in this study use a two-dimensional geometry, which does not include the displacement thickness effect of the lateral walls and so the two-dimensional geometry illustrated in the right plot of Figure 1 exhibits a tilted top wall to mimic this effect. This leads to a nearly-rectangular computational domain with a flat horizontal bottom wall and two vertical lines perpendicular to the incoming flow as the inlet and outlet boundaries.

In this study, all the surfaces of the wind tunnel and wing are hydraulically smooth with the exception of the trip wire that is used at the inlet of the tunnel, but not included in the simulations. As discussed in Fritsch et al. [2022], the inlet boundary location was tuned to obtain a

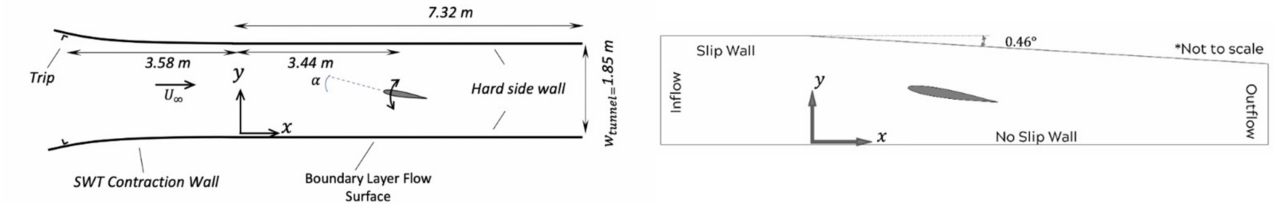

Figure 1: Illustration of the geometry tested in the Virginia Tech Stability Wind Tunnel (left plot) and of the domain proposed for the two-dimensional simulations (right plot), from Fritsch et al. [2022].

good match between simulations and experiments at the most upstream location with experimental data available, which is roughly two chord lengths upstream of the leading edge. The displacement thickness δ^* and the mean horizontal velocity component V_x profile were the variables selected to compare experiments and numerical calculations. Note that these changes of computational domain and boundary conditions are important for Validation exercises and may lead to significant input uncertainties. However, for the present exercise of quantifying differences between solutions obtained by different turbulence models, they are less important as long as they are kept fixed for all simulations.

The Reynolds number Re based on the reference velocity V_∞, airfoil chord c and kinematic viscosity of the fluid ν of the experiments is

$$Re = \frac{V_\infty c}{\nu} = 2 \times 10^6 \ .$$

Simulations are performed with $V_\infty = 1$, $c = 0.914$ and ν tuned to obtain the desired Reynolds number ($\nu = 0.914/Re$), which means that x and y coordinates are made dimensionless with a reference length of 1m. In the present study, we have also performed simulations for $Re = 10^9$, which was simply achieved keeping the same reference length and velocity and reducing ν.

5.2 Boundary conditions

There are five locations that require the specification of boundary conditions: the airfoil surface, the bottom boundary, the inlet boundary, the top boundary and the outlet boundary. In this study, we have followed the computational domain and boundary conditions suggested by Fritsch et al. [2022].

At the surface of the airfoil and at the bottom boundary the no-slip condition and the impermeability of the surface lead to exact boundary conditions for the mean velocity components. On the other hand, the pressure derivative in the direction normal to the wall is assumed to be zero $\partial p/\partial n = \nabla p \cdot \vec{n} = 0$. The challenging part of the wall boundary conditions in a turbulent flow is the determination of the shear-stress at the wall τ_w. In the present work, τ_w is determined directly from its definition (no wall functions), which leads to

$$\tau_w = \mu \frac{V_{t2}}{y_{n2}} \ , \tag{10}$$

where V_{t2} is the velocity component tangential to the wall at the near-wall cell centre and y_{n2} is the distance to the wall of the near-wall cell centre.

All turbulence quantities are equal to zero ($\tilde{\nu}_t = 0$, $k = 0$, $\sqrt{k}L = 0$ and $\overline{v_i v_j} = 0$) at the airfoil surface and bottom wall, but ω goes to infinity at these boundaries. In order to avoid the singular behavior of ω at the wall, the near-wall analytic solution of the ω transport equation Wilcox [2006] is used to specify ω at the near-wall cell centre.

At the inlet boundary, the velocity is set equal to undisturbed flow conditions, i.e. $V_x = V_\infty$ and $V_y = 0$ and the pressure is extrapolated from the interior assuming zero streamwise derivative. Turbulence kinetic energy and normal Reynolds stresses are specified from a turbulence intensity of 0.2% assuming isotropic turbulence. The values of $\tilde{\nu}_t$, ω, $\sqrt{k}L$ are derived from k and an eddy-viscosity that satisfies the empirical relation

$$\left(\frac{\nu_t}{\nu}\right)_{\text{inlet}} = 10^{-8} Re \ . \tag{11}$$

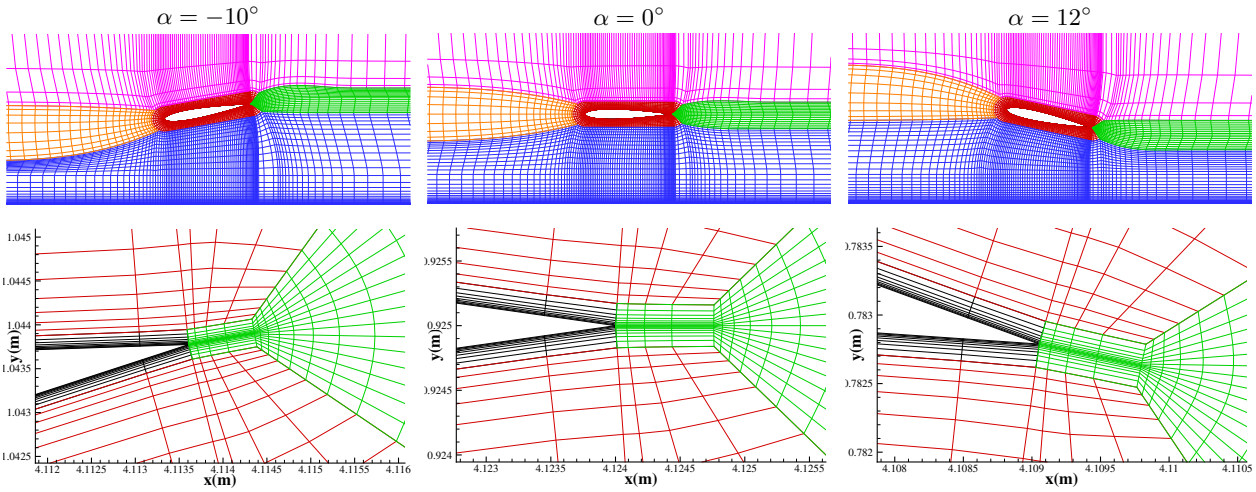

Figure 2: Illustration of the grids for the simulations of the geometry tested in the Virginia Tech Stability Wind Tunnel.

This leads to $\nu_t = 0.02\nu$ for $Re = 2 \times 10^6$ and to $\nu_t = 10\nu$ for $Re = 10^9$.

At the top boundary free slip conditions are applied which means that normal derivatives of all dependent variables are set equal to zero and that the velocity component normal to the boundary is set equal to zero. wall

At the outlet boundary, the pressure is imposed and zero streamwise derivatives are applied to the remaining dependent variables.

5.3 Grid sets

Six sets of nine geometrically similar multi-block grids with the same topology were used in this exercise, one for each angle of attack and each Reynolds number. The direct calculation of the shear-stress at the wall from equation (10) requires different near-wall spacing for the two Reynolds numbers tested.

The nine grids of each set are generated with one-dimensional (along each family of grid lines) cubic interpolations performed in each of the blocks of a basis grid that was generated with the algebraic, hyperbolic and elliptic grid generators described in Eça et al. [2002]. The grids include a region of orthogonal Cartesian lines in the vicinity of the bottom wall and views of much coarser grids than those used in this study are presented in Figure 2. The sets of grids for the two Reynolds numbers differ only on the grid node distribution along the normal grid lines to the surfaces where the no-slip condition is applied. The Vinokur [1983] stretching functions are used to tune the height of the near-wall cells, which is presented in wall coordinates $(y^+_{n2})_{\max}$ in Table 1. The values of $(y^+_{n2})_{\max}$ are from the SST03 simulations with the airfoil at angle of attack of 12°. Similar values are obtained for the other two angles of attack and for the remaining five turbulence models. In the finest grids of the two sets, the number of cells in the linear sub-layer ($y^+ < 5$) of the bottom wall boundary-layer at $x = 1.25$ is 19 for $Re = 2 \times 10^6$ and 13 for $Re = 10^9$. At the same location, there are 76 cells for $Re = 2 \times 10^6$ and 46 cells for $Re = 10^9$ in the viscous sub-layer ($y^+ < 50$). The number of cells across the boundary-layer (total head below 0.99) is 228 for $Re = 2 \times 10^6$ and 210 for $Re = 10^9$.

Table 1 also presents the total number of cells of each grid N_{cells}, the number of faces on the bottom wall $(N_f)_{\text{bottom}}$, the number of faces on the airfoil surface $(N_f)_{\text{airfoil}}$ and the grid refinement ratio $r_i = h_i/h_1$. In these geometrically similar grids, the grid refinement ratio can be calculated from

$$r_i = h_i/h_1 = \left(\frac{(N_1)_{\text{cells}}}{(N_i)_{\text{cells}}} \right)^{1/2} = \frac{(N_{f1})_{\text{bottom}}}{(N_{fi})_{\text{bottom}}} = \frac{(N_{f1})_{\text{airfoil}}}{(N_{fi})_{\text{airfoil}}} \ . \tag{12}$$

Table 1: Number of cells N_{cells}, number of cell faces on the bottom wall $(N_f)_{\text{bottom}}$, number of cell faces on the airfoil surface $(N_f)_{\text{airfoil}}$, grid refinement ratio r_i and $(y^+_{n2})_{\max}$. $(y^+_{n2})_{\max}$ obtained with the SST03 turbulence model for the NACA 0012 airfoil at $\alpha = 12°$.

	$Re = 2 \times 10^6$ and $Re = 10^9$				$(y^+_{n2})_{\max}$			
					$Re = 2 \times 10^6$		$Re = 10^9$	
Grid	N_{cells}	$(N_f)_{\text{bottom}}$	$(N_f)_{\text{airfoil}}$	r_i	Bottom	Airfoil	Bottom	Airfoil
1	839,680	1,152	1,024	1.00	0.17	0.09	0.19	0.08
2	554,320	936	832	1.23	0.20	0.11	0.23	0.10
3	396,880	792	704	1.45	0.23	0.13	0.27	0.12
4	265,880	648	576	1.78	0.27	0.16	0.32	0.14
5	209,920	576	512	2.00	0.30	0.18	0.36	0.16
6	138,580	468	416	2.46	0.36	0.23	0.44	0.20
7	99,220	352	352	2.91	0.41	0.28	0.51	0.24
8	66,470	288	288	3.56	0.49	0.35	0.62	0.30
9	52,480	256	256	4.00	0.54	0.40	0.69	0.34

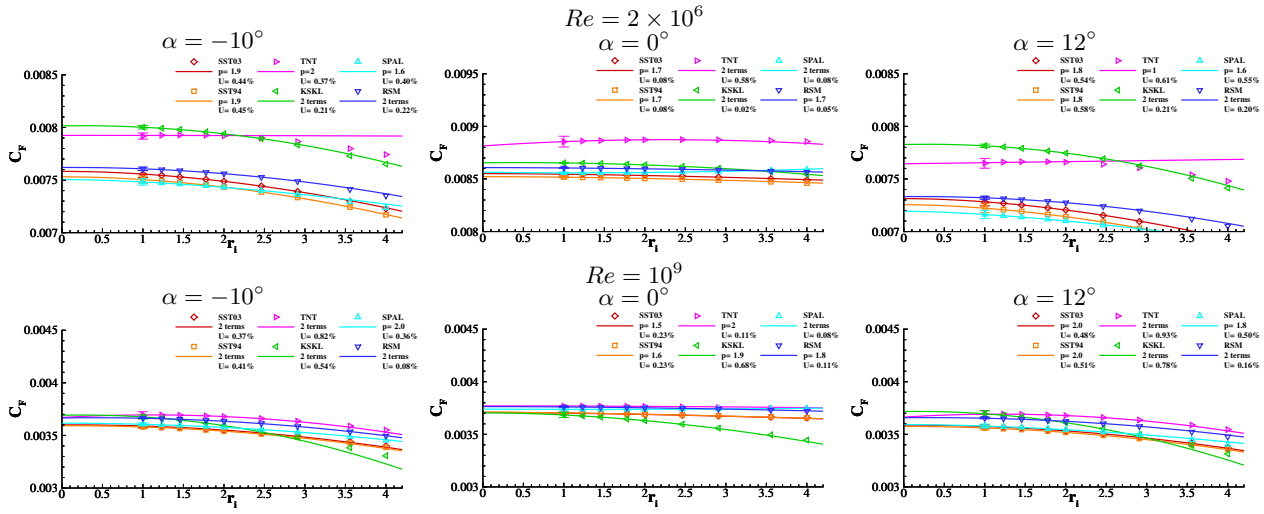

Figure 3: Convergence of the friction drag coefficient C_F of the airfoil with grid refinement.

5.4 Simulations settings

Calculations were all performed in double-precision (14 digits) and iterative convergence criteria requires a maximum value of the normalized residual of all transport equations below 10^{-9}, which guarantees that the numerical uncertainty is dominated by the contribution of the discretization error. All the results presented below are from simulations that satisfied the present iterative convergence criteria.

Numerical uncertainties are estimated with an updated version described in Eça et al. [2023] of the procedure presented in Eça and Hoekstra [2014]. Power series expansions with estimated or imposed order of grid convergence p are used to estimate the numerical error. In cases of non-monotonic convergence, a power series expansion with first and second order terms is used (designated by 2 terms). In the present study, all fits are based on the data of the five finest grids. Nonetheless, results from the coarsest grids will also be presented to illustrate the grid convergence properties obtained with the different turbulence models and Reynolds numbers.

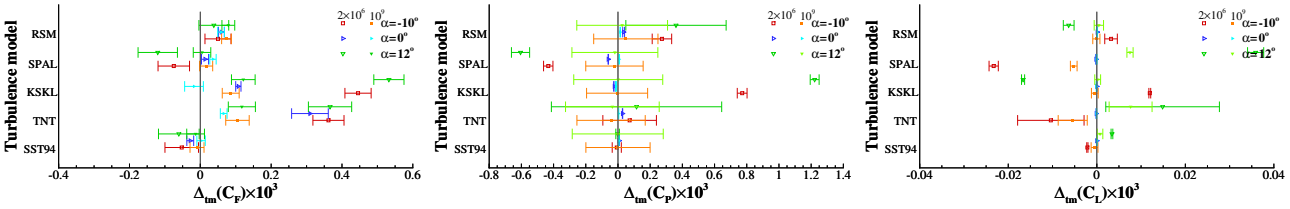

Figure 4: Point-wise Validation metric for the friction drag coefficient C_F, pressure drag coefficient C_P and lift coefficient C_L. Reference solution obtained with the SST03 turbulence model.

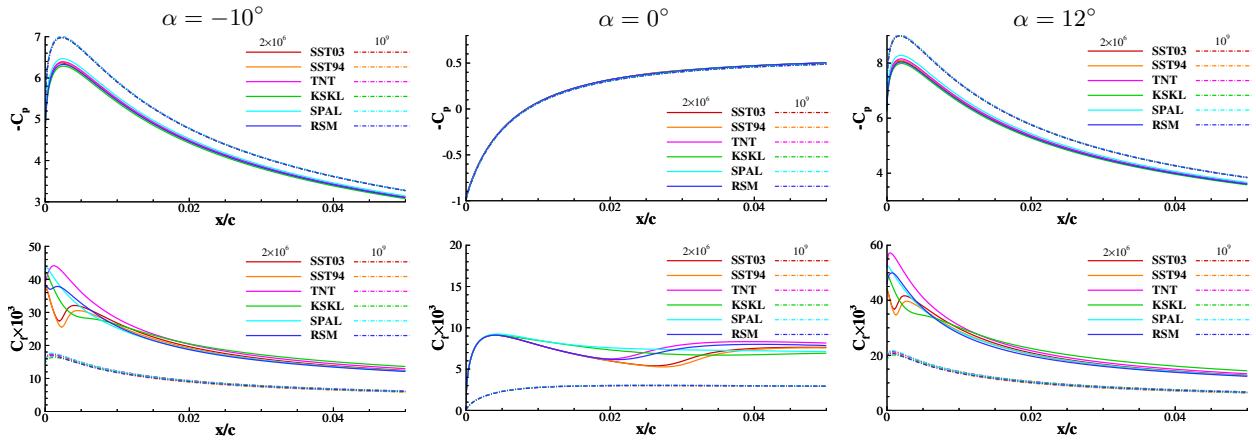

Figure 5: Pressure coefficient C_p and skin friction C_f coefficients at the leading edge of the airfoil obtained in the finest grids. Lower surface for $\alpha = -10°$ and $\alpha = 0°$ and upper surface for $\alpha = 12°$.

6. RESULTS

6.1 Airfoil

The friction C_F and pressure C_P drag coefficients and the lift C_L coefficient are the integral quantities of interest determined from the flow around the airfoil. The local quantities of interest are the skin friction C_f and pressure C_p coefficients on the surface of the airfoil calculated at 78 locations on the airfoil surface by cubic interpolation.

Figure 3 presents the convergence of C_F with grid refinement for the three angles of attack and two Reynolds numbers. It is clear that the discrepancies between the solutions of the six turbulence models are larger at $Re = 2 \times 10^6$ than at $Re = 10^9$. For the present level of grid refinement, there are several cases that do not exhibit monotonic convergence. Nonetheless, estimated numerical uncertainties are all below 1% and most of them below 0.5%.

The application of the point-wise V&V20 [2009] Validation metric to quantify the discrepancies between C_F, C_P and C_L obtained with the six turbulence models is illustrated in Figure 4. For the present level of grid refinement, there is still a significant numerical uncertainty in the determination of C_P. Nevertheless, the discrepancies between C_F, C_P and C_L obtained with different turbulence models are smaller at $Re = 10^9$ than at $Re = 2 \times 10^6$ for all angles of attack with the exception of C_F for the RSM model. With the RSM model, the largest $\Delta_{\text{tm}}(C_F)$ are observed for the highest Reynolds number.

Figure 5 presents the C_p and C_f distributions at the leading edge of the airfoil obtained in the finest grids. Results are for the lower surface at $\alpha = -10°$ and $\alpha = 0°$ and for the upper surface at $\alpha = 12°$. Even graphically, it is possible to identify the reduction of discrepancies between turbulence models with the increase of the Reynolds number. As expected, the largest differences are obtained for C_f at the transition from laminar to turbulent flow, which is only visible for $Re = 2 \times 10^6$. A quantitative assessment of the differences between turbulence models is presented in Figure 6 that presents $\Delta_{\text{tm}}(C_p)$ and $\Delta_{\text{tm}}(C_f)$ at the 78 selected locations on the surface of the

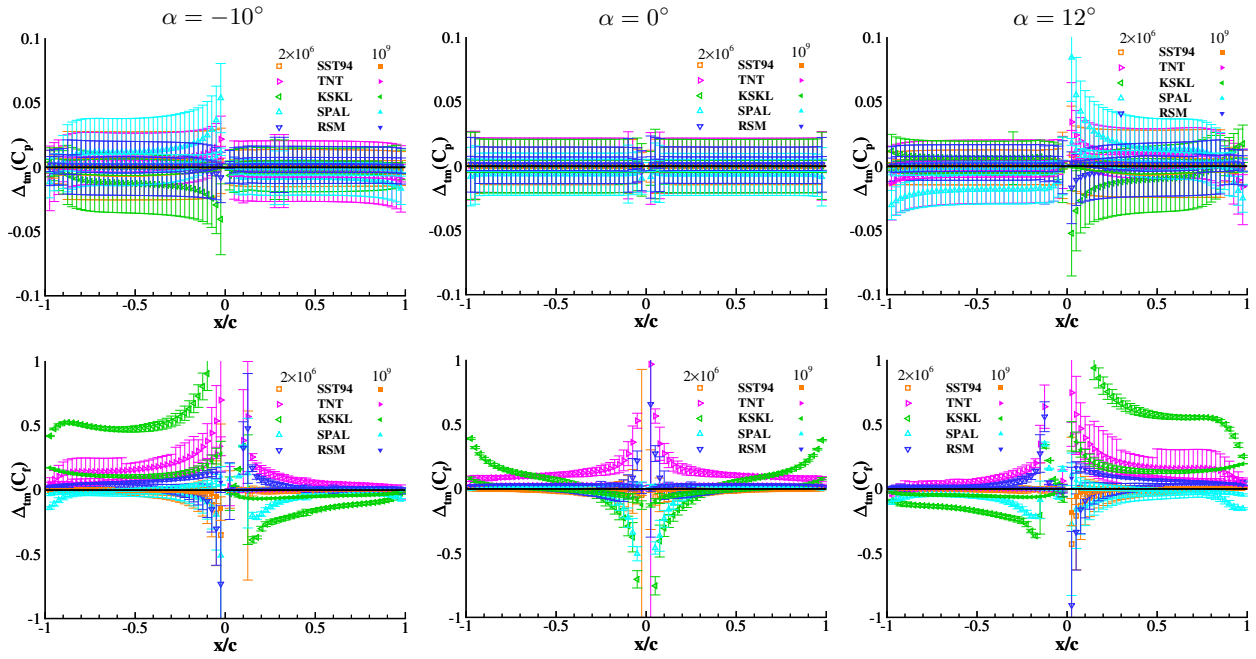

Figure 6: Point-wise Validation metric for the pressure coefficient C_p and skin friction C_f coefficient on the airfoil. Coordinates x/c of the lower surface are negative. Reference solution obtained with the SST03 turbulence model.

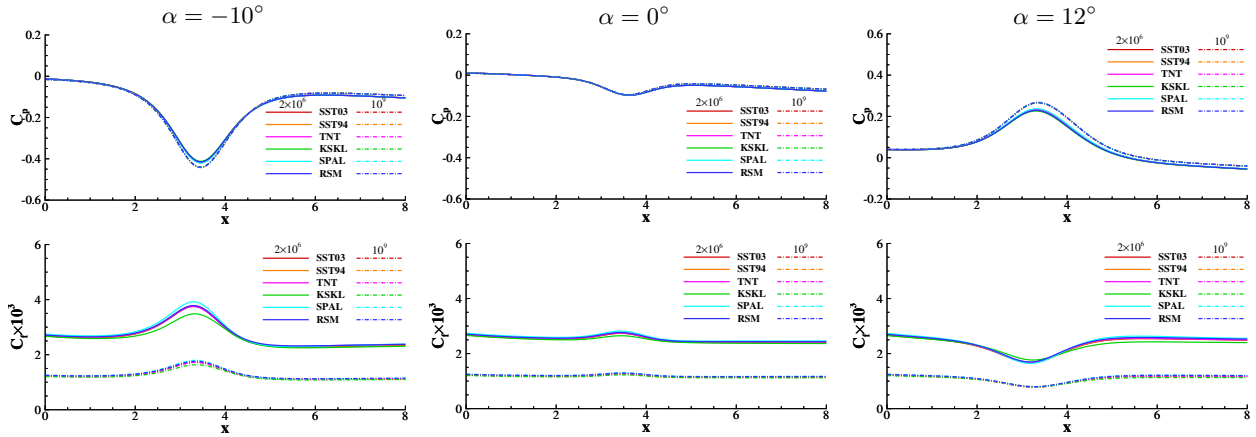

Figure 7: Pressure coefficient C_p and skin friction C_f coefficients on the wind tunnel wall obtained in the finest grids.

airfoil. Coordinates x/c of the lower surface are set negative for illustration purposes.

The main trends observed in the data plotted in Figure 6 are: the choice of turbulence model affects more C_f than C_p ($\Delta_{\text{tm}}(C_f) > \Delta_{\text{tm}}(C_p)$), but for the eddy-viscosity models, the values of $\Delta_{\text{tm}}(C_f)$ are significantly smaller for the highest Reynolds number; the opposite trend observed for the RSM model in C_F is a consequence of the adverse pressure gradient boundary-layer; the largest discrepancies are observed at the locations of transition from laminar to turbulent flow, which also exhibit the largest numerical uncertainties.

6.2 Boundary-layer on the wind tunnel wall

The quantities of interest for the boundary-layer on the wind tunnel wall are: pressure coefficient C_p, skin friction coefficient C_f, displacement thickness δ^*, momentum thickness θ, mean horizontal

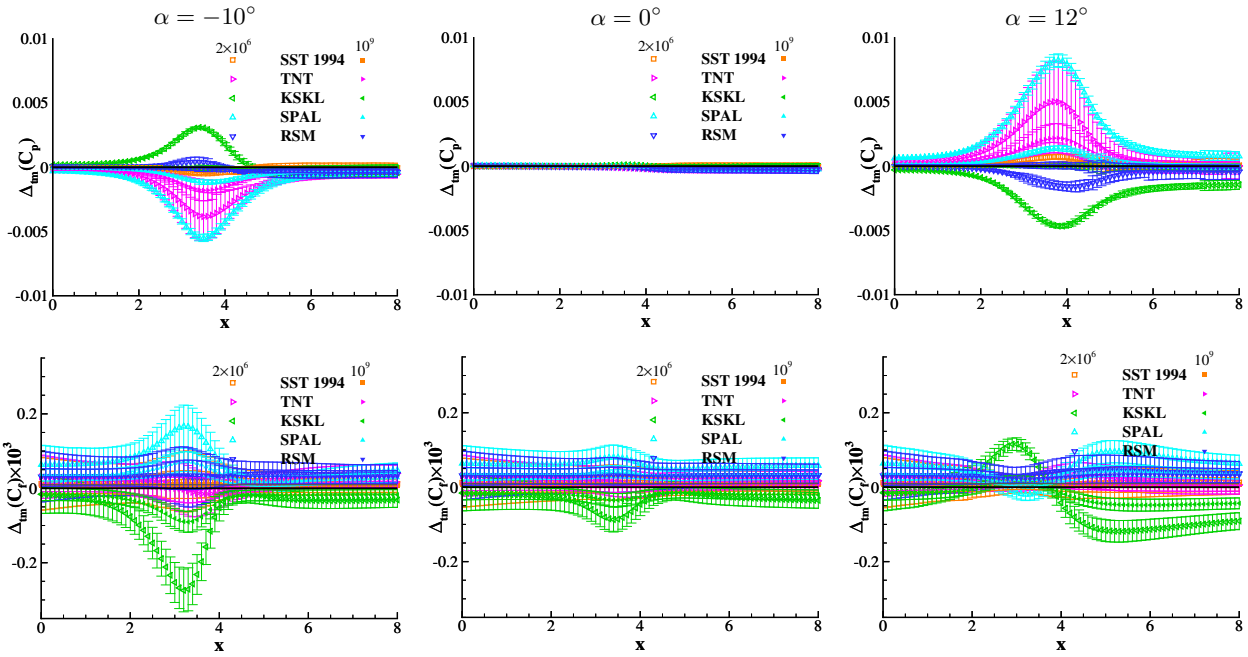

Figure 8: Point-wise Validation metric for the pressure coefficient C_p and skin friction C_f coefficient on the wind tunnel wall. Reference solution obtained with the SST03 turbulence model.

velocity component V_x, turbulence kinetic energy k and Reynolds-stress $\overline{v_x v_y}$ (in the plots we will omit the overbar). These quantities are calculated at 81 equally spaced locations between $0 \leq x \leq 8$.

C_f and C_p are obtained by cubic interpolation. δ^* and θ are determined with a second-order trapezoidal rule of local V_x profiles obtained by cubic interpolation.

$$\delta^* = \int_0^{y_{\text{ext}}} \left(1 - \frac{V_x}{V_{xe}}\right) \mathrm{d}y \tag{13}$$

and

$$\theta = \int_0^{y_{\text{ext}}} \left(\frac{V_x}{V_{xe}} - \left(\frac{V_x}{V_{xe}}\right)^2\right) \mathrm{d}y \ . \tag{14}$$

The external velocity V_{xe} required to determine δ^* and θ at each value of x along the bottom wall is obtained from V_x at the point with the largest total head (or stagnation pressure) y_{ext}.

V_x, k and $\overline{v_x v_y}$ are determined at 100 locations of the 81 cross-sections using cubic interpolation. The selected locations are equidistant in log scale with the nearest location at $y^+_{n2} = 2$ and the top location is at y_{ext}. These coordinates are determined for the finest grid of each Reynolds number from the SST03 model results and kept fixed for the remaining grids and turbulence models of the same Reynolds number.

Figure 7 compares the C_p and C_f distributions on the wind tunnel wall obtained in the finest grids with the six turbulence models, three angles of attack and two Reynolds numbers. The differences between the solutions seem to be smaller than those obtained on the airfoil surface and only the KSKL and SPAL solutions at the lowest Reynolds number show graphical discrepancies. These trends are confirmed in Figure 8 that presents $\Delta_{\text{tm}}(C_p)$ and $\Delta_{\text{tm}}(C_f)$. Note that the vertical scales are different than those used in Figure 6.

Figure 9 presents the evolution of δ^* and θ of the boundary-layer on the wind tunnel wall obtained in the finest grids. The solutions of the six turbulence models are very similar for the three angles of attack and two Reynolds numbers. The values of $\Delta_{\text{tm}}(\delta^*)$ and $\Delta_{\text{tm}}(\theta)$ plotted in Figure 10 are all within the numerical uncertainty confirming that differences in δ^* and θ cannot be quantified for the present level of grid refinement.

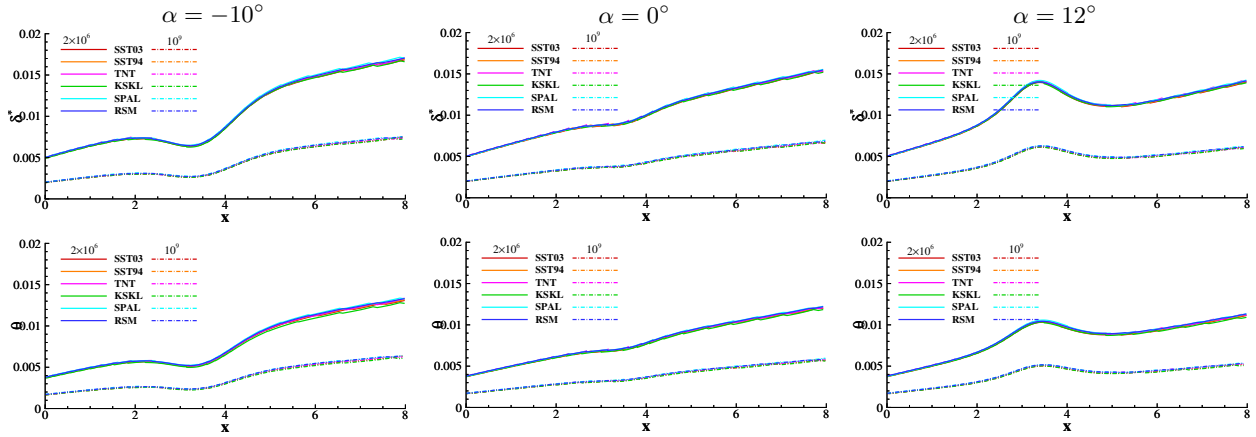

Figure 9: Displacement thickness δ^* and momentum thickness θ of the boundary-layer on the wind tunnel wall obtained in the finest grids.

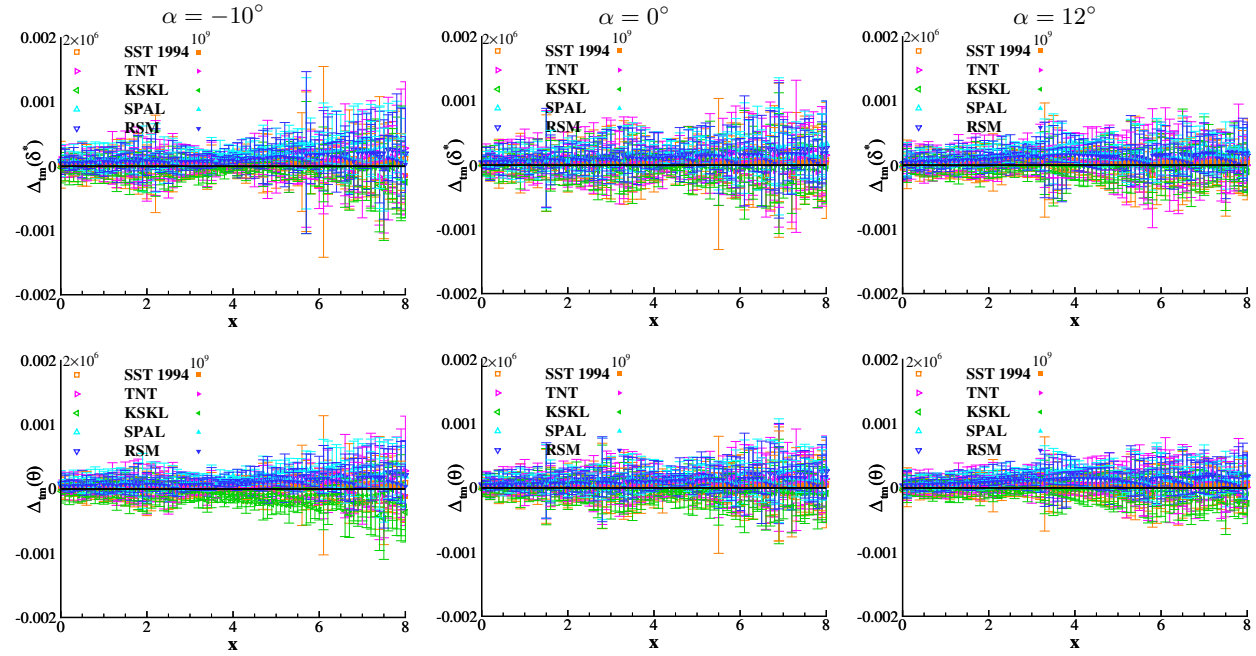

Figure 10: Point-wise Validation metric for the displacement thickness δ^* and momentum thickness θ of the boundary-layer on the wind tunnel wall. Reference solution obtained with the SST03 turbulence model.

The mean horizontal velocity component V_x profiles obtained in the finest grids at $x = 3.5$ are plotted in Figure 11 in wall coordinates. At this location, there is a favorable pressure gradient for $\alpha = -10°$ and an adverse pressure gradient for $\alpha = 12°$. The data show the following trends: the differences between the solutions of the six turbulence models are difficult to identify graphically; nonetheless, the largest differences are obtained for the KSKL and SPAL model in the buffer-layer and in the outer-layer of the boundary-layer; the log-law region is significantly larger at $Re = 10^9$ than at $Re = 2 \times 10^6$ for the three angles of attack.

In simulations performed without wall functions, the shear-stress at the wall (friction velocity) is determined from its definition, equation (10). Therefore, it is possible to determine the Von Kármán constant κ from a linear fit to the velocity profile in the log-law region.

$$\frac{V_x}{u_\tau} = \frac{1}{\kappa} \ln\left(\frac{u_\tau y}{\nu}\right) + C \,, \tag{15}$$

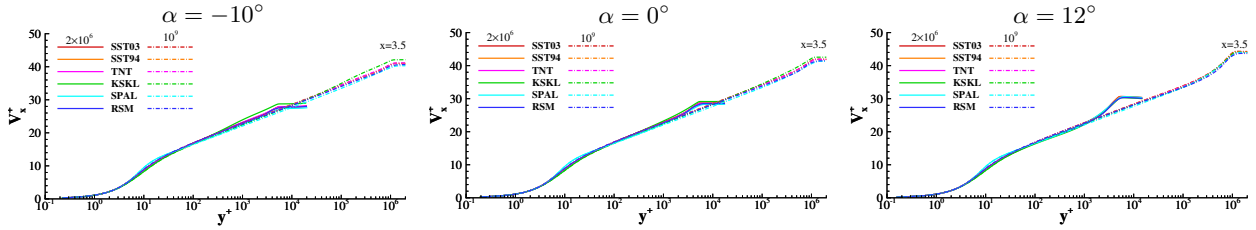

Figure 11: Mean horizontal velocity component V_x profiles obtained in the finest grids in wall coordinates at $x = 3.5$ of the boundary-layer on the wind tunnel wall.

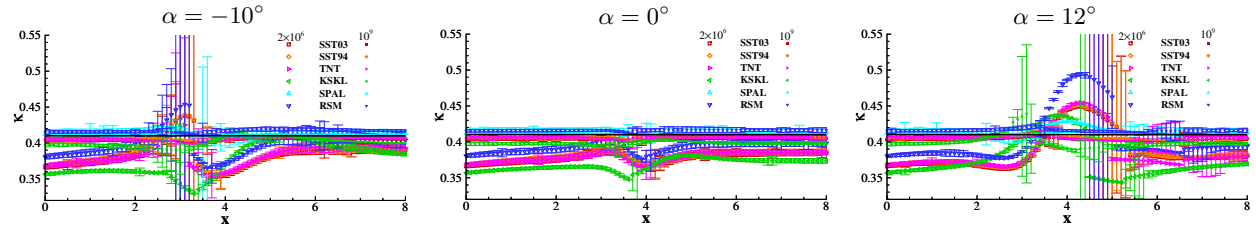

Figure 12: Von Kármán constant κ obtained from linear fits to the log-law region of the mean horizontal velocity component V_x profiles of the boundary-layer on the wind tunnel wall.

where $u_\tau = \sqrt{\tau_w/\rho}$ and C is a constant and so the slope of the fit determines κ.

The results obtained from the velocity profiles of the boundary-layers on the wind tunnel wall are depicted in Figure 12. There is a significant effect of the Reynolds number on the value of κ obtained from the six turbulence models. At $Re = 2 \times 10^6$, the pressure gradient has a strong influence on the value of κ for all turbulence models except the SPAL model that exhibits the values closest to the expected value of 0.41. For the remaining five models the values of κ are below 0.41 for most of the locations and tend to decrease in adverse pressure gradient. On the other hand, κ increases for favorable pressure gradient regions and for $\alpha = 12°$ the effect is visible also for the SPAL model.

All the turbulence models show much less sensitivity to the pressure gradient at $Re = 10^9$. Furthermore, the values of κ are all much closer to 0.41 than for the lowest Reynolds number.

Figure 13 presents the turbulence kinetic energy k profiles obtained in the finest grids at $x = 3.5$ in wall coordinates. There are graphical differences for the KSKL and SPAL solutions for both Reynolds numbers. However, there is a significant influence of the Reynolds number on the k profile shape in the log-law region. The expected plateau at $k^+ = 1/\sqrt{c_\mu} \approx 3.3$ is only obtained for the highest Reynolds number. This result is confirmed by the value of $(k^+)_{\max}$ in the log-law region ($30 \leq y^+_{n2} =\leq 110$ for $Re = 2 \times 10^6$ and $10^2 \leq y^+_{n2} =\leq 10^4$ for $Re = 10^9$) plotted in Figure 14. Furthermore, for $Re = 2 \times 10^6$ there is a strong influence of the favorable pressure gradient on $(k^+)_{\max}$ that is not as pronounced at $Re = 10^9$.

Figure 15 presents the Reynolds-stress $\overline{v_x v_y}$ profiles obtained in the finest grids at $x = 3.5$ in wall coordinates. The trends observed in the $\overline{v_x v_y}$ profiles are similar to those discussed above for k. In this case, the expected value of the Reynolds-stress in the log-law region is $(\overline{v_x v_y})^+ \simeq 1$. Figure 16 presents $(\overline{v_x v_y})^+_{\max}$ for the same range of y^+_{n2} used to determine $(k^+)_{\max}$. The results show again a larger influence of the pressure gradient at $Re = 2 \times 10^6$ than at $Re = 10^9$. Furthermore, for the highest Reynolds number all turbulence models lead to very similar values of $(\overline{v_x v_y})^+_{\max}$, which are very close to 1.

6.3 Global assessment

The multivariate metric proposed in V&V20.1 [2023] was applied to all quantities of interest discussed above for the airfoil and boundary-layer of the wind tunnel wall, except the force coefficients of the airfoil. As mentioned above, the reference results are taken from the solution obtained with the SST03 turbulence model and $\Delta_{\text{mv}}/\Delta_{\text{ref}}$ quantifies the discrepancies to the other five turbulence

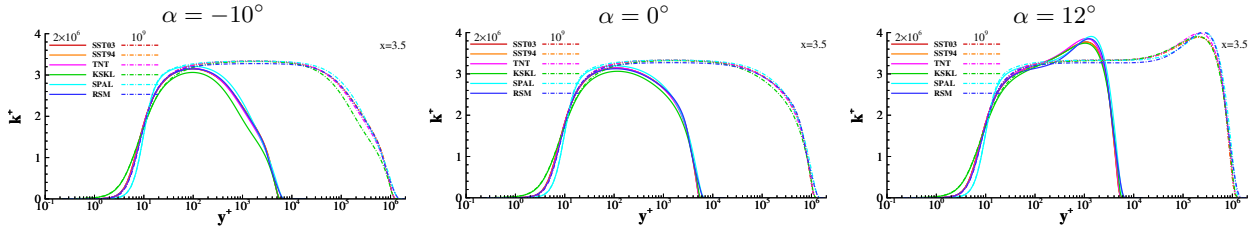

Figure 13: Turbulence kinetic energy k profiles obtained in the finest grids in wall coordinates at $x = 3.5$ of the boundary-layer on the wind tunnel wall.

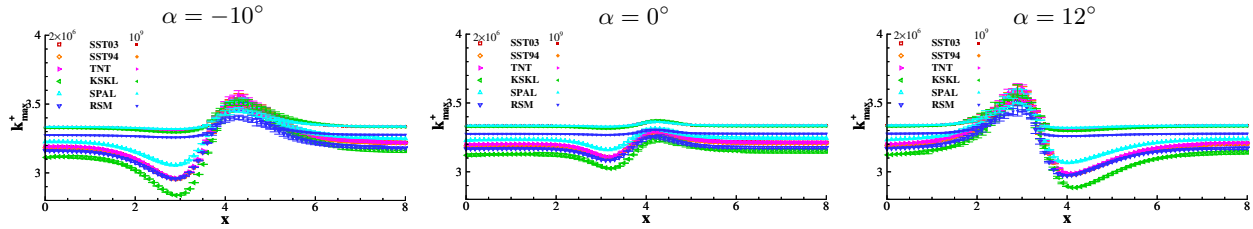

Figure 14: Maximum turbulence kinetic energy in the log-law region ($30 \leq y^+_{n2} =\leq 110$ for $Re = 2 \times 10^6$ and $10^2 \leq y^+_{n2} =\leq 10^4$ for $Re = 10^9$) of the boundary-layer on the wind tunnel wall.

models taking into account the numerical uncertainties.

The values of $\Delta_{\text{mv}}/\Delta_{\text{ref}}$ are plotted in Figure 17 for the three angles of attack and two Reynolds numbers tested. The data confirms that discrepancies between turbulence models are smaller at $Re = 10^9$ than at $Re = 2\times10^6$ with the exception of C_f for the airfoil surface with the RSM model, which has been identified above. Nonetheless, there are some details that have to be interpreted carefully. The largest values of $\Delta_{\text{mv}}/\Delta_{\text{ref}}$ are obtained for C_p on the wind tunnel wall, which seems an unexpected result. However, numerical uncertainties for this flow quantity are the smallest of all the selected quantities of interest and so $\Delta_{\text{mv}}/\Delta_{\text{ref}}$ is just indicating that the discrepancies between turbulence models solutions are significantly larger than the numerical uncertainties. Furthermore, the metric is indicating which are the turbulence models that show the largest discrepancies to the reference solution for this quantity of interest.

A similar effect of the numerical uncertainty is observed for the V_x, k and $\overline{v_x v_y}$ profiles. For most turbulence models, the largest values of $\Delta_{\text{mv}}/\Delta_{\text{ref}}$ are obtained for V_x, which does not mean that the discrepancies in the mean horizontal component are smaller than those obtained for the turbulence quantities. Although it was not presented in the previous section, numerical uncertainties estimated for k and $\overline{v_x v_y}$ are larger than those obtained for V_x.

7. CONCLUSIONS

This paper presents a quantitative assessment of the influence of the Reynolds number on the difference between results of CFD simulations performed with RANS using six different turbulence models: five eddy-viscosity models, Spalart & Allmaras one-equation model, SST 1994, SST 2003 and TNT $k-\omega$ two-equation models and $k-\sqrt{k}L$ two-equation model, and the SSG-LRR$-\omega$ Reynolds-stress model.

The test cases are boundary-layers under non-equilibrium pressure gradient that were measured in the Virginia Tech wind tunnel at a Reynolds number of $Re = 2 \times 10^6$. The pressure gradient is induced by a rectangular wing with a NACA 0012 section at angles of attack of $-10°$, $0°$ and $12°$.

The simulations are performed for $Re = 2 \times 10^6$ and $Re = 10^9$ in a two-dimensional domain for a Newtonian incompressible fluid. Shear-stress at the wall is determined directly from its definition for both Reynolds numbers, i.e. simulations are performed without wall functions. Sets of nine geometrically similar grids were used for all flow settings and turbulence models to enable the estimation of numerical uncertainties.

The quantities of interest are: force coefficients, skin friction and pressure coefficient distribu-

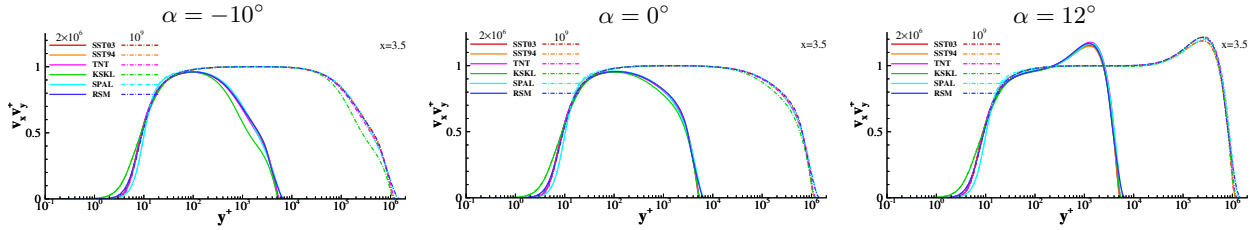

Figure 15: Reynolds-stress $\overline{v_x v_y}$ profiles obtained in the finest grids in wall coordinates at $x = 3.5$ of the boundary-layer on the wind tunnel wall.

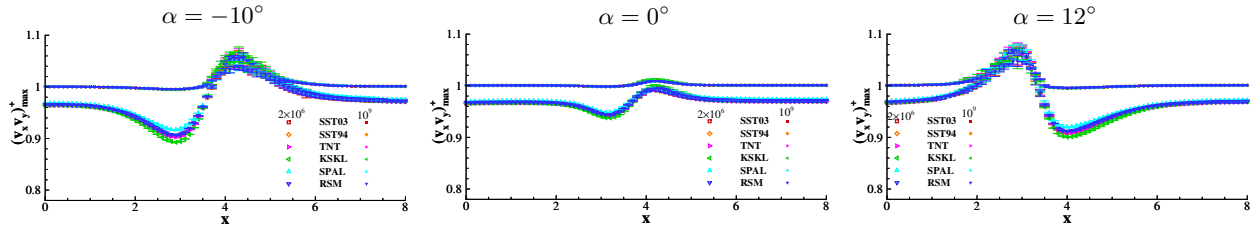

Figure 16: Maximum Reynolds-stress in the log-law region ($30 \leq y^+_{n2} =\leq 110$ for $Re = 2 \times 10^6$ and $10^2 \leq y^+_{n2} =\leq 10^4$ for $Re = 10^9$) of the boundary-layer on the wind tunnel wall.

tions on the surface for the airfoil; skin friction and pressure coefficient distributions, displacement and momentum thicknesses evolution and mean horizontal velocity, turbulence kinetic energy and Reynolds-stresses profiles of the boundary-layer on the wind tunnel wall. For all these quantities, Validation metrics are used to quantify the differences between the solutions obtained with the six turbulence models. The SST 2003 results are used as the reference solution ("experimental data") to determine the comparison error of the other five models. Validation uncertainties are determined from the numerical uncertainties.

The results obtained in this study show for almost all quantities of interest significantly larger differences between the results of the six turbulence models at $Re = 2 \times 10^6$ than at $Re = 10^9$. The two exceptions are: the C_f distribution on the airfoil surface obtained with the SSG-LRR$-\omega$ model that shows largest differences to the $k-\omega$ SST 2003 for the highest Reynolds number; the displacement and momentum thicknesses of the wind tunnel boundary-layers that exhibit differences between the six turbulence models that are smaller than the numerical uncertainty for both Reynolds numbers.

The analysis of the V_x, k and $\overline{v_x v_y}$ profiles showed a strong effect of the pressure gradient on the log-law region for $Re = 2 \times 10^6$ and five of the turbulence models tested. The Von Kármán constant κ determined from the V_x profiles is not equal to 0.41 and its value changes with the pressure gradient. For the Spalart & Allmaras model κ is close to 0.41 and the effect of the pressure gradient is weakest and mainly observed for favorable pressure gradient. Similar trends are observed for the k and $\overline{v_x v_y}$ profiles in the log-law region.

At $Re = 10^9$ all turbulence models lead to values of κ much closer to 0.41 and there is almost no influence of the pressure gradient on the profiles of V_x, k and $\overline{v_x v_y}$ profiles in the log-law region.

The present exercise suggests that model error assessments (Validation) performed at model scale cannot be extrapolated to full scale. Furthermore, the small discrepancies obtained between the solutions of six turbulence models at full scale is encouraging. The ability to simulate full scale conditions, for which there is almost no experimental data available, is one of the biggest assets of CFD.

References

L. Eça and M. Hoekstra. A procedure for the estimation of the numerical uncertainty of CFD calculations based on grid refinement studies. *Journal of Computational Physics*, 262:104–130, 2014.

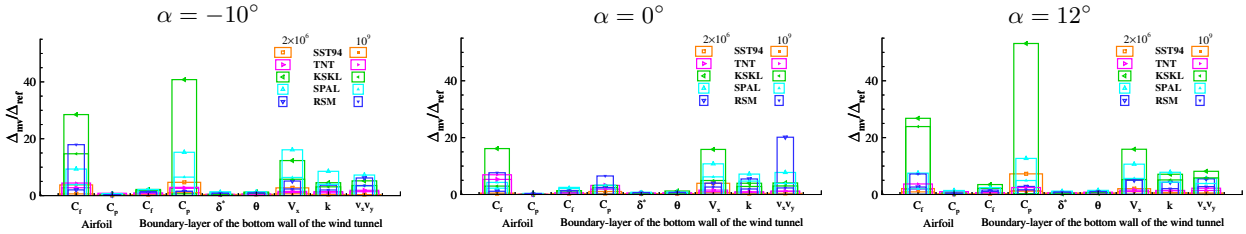

Figure 17: Multivariate metric applied to the quantities of interest of the airfoil and boundary-layer on the wind tunnel wall. Reference results are taken from the solution obtained with the SST03 turbulence model.

L. Eça, M. Hoekstra, and J. Windt. Practical Grid Generation Tools with Applications to Ship Hydrodynamics. In 8^{th} *International Conference on Numerical Grid Generation in Computational Field Simulations, Honolulu, Hawaii, U.S.A.*, 2002.

L. Eça, C.M. Klaij, G. Vaz, M. Hoekstra, and F.S. Pereira. On code verification of RANS solvers. *Journal of Computational Physics*, 310:418–439, 2016. doi: https://doi.org/10.1016/j.jcp.2016.01.002. URL `https://www.sciencedirect.com/science/article/pii/S0021999116000036`.

L. Eça, M. Kerkvliet, and S.L Toxopeus. Simulation of 2D Smooth Wall Turbulent Boundary Layers with Variable Pressure Gradient using RANS. Technical Report M-10, IST, 2022.

L. Eça, S.L Toxopeus, and M. Kerkvliet. Procedures for the estimation of numerical uncertainties in the simulation of steady and unsteady flows. Technical Report M-8, IST, April 2023.

B. Eisfeld, C. Rumsey, and V. Togiti. Verification and validation of a second-moment-closure model. *AIAA Journal*, 54(5):1524–1541, 2016. doi: 10.2514/1.J054718. URL `https://doi.org/10.2514/1.J054718`.

D. Fritsch, V. Vishwanathan, J. Duetsch-Patel, A. Gargiulo, K.T. Lowe, and W.J. Devenport. The pressure signature of high reynolds number smooth wall turbulent boundary layers in pressure gradient family. In *AIAA AVIATION 2020 FORUM*, 2020. doi: 10.2514/6.2020-3066. URL `https://arc.aiaa.org/doi/abs/10.2514/6.2020-3066`.

D. Fritsch, V. Vishwanathan, C.J. Roy, K.T. Lowe, W.J. Devenport, Y. Nishi, T.A. Knopp, P. Stroer, A. Krumbein, R.D. Sandberg, C. Lav, R. Bensow, L. Eça, S.L. Toxopeus, M. Kerkvliet, M. Slama, and L. Bordier. *Experimental and Computational Study of 2D Smooth Wall Turbulent Boundary Layers in Pressure Gradient*, chapter AIAA SCITECH 2022 Forum. 2022. doi: 10.2514/6.2022-0696. URL `https://arc.aiaa.org/doi/abs/10.2514/6.2022-0696`.

C. M. Klaij and C. Vuik. Simple-type preconditioners for cell-centered, collocated finite volume discretization of incompressible Reynolds-averaged Navier-Stokes equations. *International Journal for Numerical Methods in Fluids*, 71(7):830–849, 2013.

J. C. Kok. Resolving the dependence on freestream values for the k- turbulence model. *AIAA Journal*, 38(7):1292–1295, 2000. doi: 10.2514/2.1101.

F. R. Menter. Two-equation eddy-viscosity turbulence models for engineering applications. *AIAA Journal*, 32(8):1598–1605, 1994. doi: 10.2514/3.12149. URL `https://doi.org/10.2514/3.12149`.

F. R. Menter, M. Kuntz, R. Langtry, Y. Nagano, M. J. Tummers, and K. Hanjalic. Ten Years of Industrial Experience with the SST Turbulence Model. In 4^{th} *Internal Symposium, Turbulence, Heat and Mass Transfer*, volume 4, pages 625–632, New York, 2003. Begell House,;. ISBN 1567001963.

F.R. Menter, Y. Egorov, and D. Rusch. Steady and unsteady flow modelling using the $k - \sqrt{kl}$ model. 2006. doi: 10.1615/ICHMT.2006.TurbulHeatMassTransf.800.

T.F. Miller and F. W. Schmidt. Use of a pressure-weighted interpolation method for the solution of the incompressible Navier-Stokes equations on a nonstaggered grid system. *Numerical Heat Transfer*, 14(2):213–233, 1988.

P.R. Spalart and S.R. Allmaras. A One-Equation Turbulence Model for Aerodynamic Flows. In *AIAA 30$^{\text{th}}$ Aerospace Sciences Meeting, Reno, U.S.A.*, 1992.

M. Vinokur. On One-Dimensional Stretching Functions for Finite-Difference Calculations. *Journal of Computational Physics*, 50(2):215–234, 1983.

ASME V&V20. *Standard for Verification and Validation in Computational Fluid Dynamics and Heat Transfer*. American Society of Mechanical Engineers, 2009.

ASME V&V20.1. *Multivariate Metric for Validation*. American Society of Mechanical Engineers, 2023.

D. C. Wilcox. *Turbulence Modeling for CFD*. DCW Industries, 3rd edition, 2006.